RESEARCH ARTICLE

ADVANCED
ELECTRONIC
MATERIALS
Open Access

www.advelectronicmat.de

Origami-Enabled Stretchable Electrodes Based on Parylene Deposition and 3D Printing

Fulvia Del Duca, Lukas Hiendlmeier, Reem Al Fata, George Al Boustani, Inola Kopic, Hu Peng, Beatrice De Chiara, Marta Nikić, Francisco Zurita, Tetsuhiko Teshima, and Bernhard Wolfrum*

Thin film electronic devices based on flexible biocompatible substrates are desired in various fields such as implants, soft robotics, and wearables, where stretchability is often necessary. Structure-enabled stretchability in flexible thin films can be achieved by introducing origami-inspired folds, thereby storing excess material in the out-of-plane direction to unfold upon stress. When using vapor-deposited substrates such as parylene-C, folds can be introduced prefabrication using molds patterned in repeated grooves and ridges. Here, this work reports the fabrication and parametrization of 10-µm-thick stretchable origami parylene-C electrodes using 3D printed molds. The molds are printed with a sinusoidal pattern and tunable amplitude and slope, with accurate printing results up to 60° steepness. A 160-nm-thick gold layer on top of the folded parylene is patterned via laser ablation following the 3D mold shape. Depending on the design parameters, the resulting electrodes maintain functionality until 40%–100% strain. By 3D printing the molds, this technique can fabricate electrodes with complete control of the designed directions of stretchability in a rapid prototyping approach.

1. Introduction

In recent years, stretchable electronics has gained significant interest for a variety of applications, including skin electronics,[1,2]
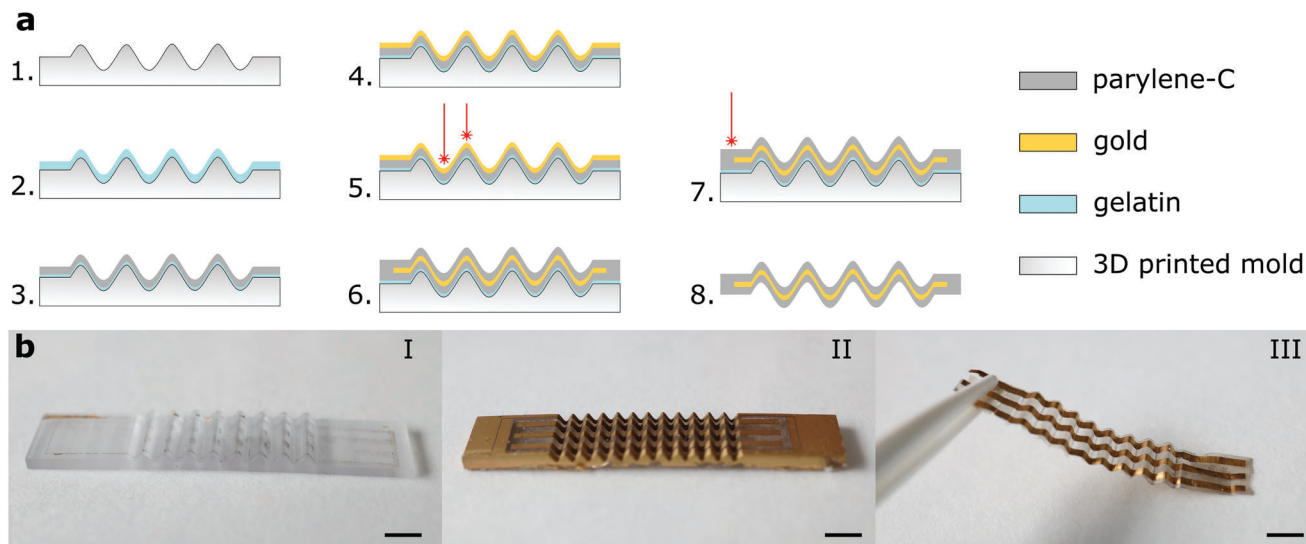
F. Del Duca, L. Hiendlmeier, R. Al Fata, G. Al Boustani, I. Kopic, H. Peng, B. De Chiara, M. Nikić, F. Zurita, T. Teshima, B. Wolfrum
Neuroelectronics
Munich Institute of Biomedical Engineering
TUM School of Computation
Information and Technology
Technical University of Munich
Hans-Piloty-Str. 1, 85748 Garching, Germany
E-mail: bernhard.wolfrum@tum.de

T. Teshima, B. Wolfrum
Medical and Health Informatics Laboratories
NTT Research Incorporated 940 Stewart Dr
Sunnyvale, CA 94085, USA

wearable monitoring systems,[3,4] invasive electrophysiological recordings,[5–8] soft robotics, and prosthetics.[9,10] One way to achieve stretchability is by using intrinsically elastic substrate materials, such as silicones[11–13] or hydrogels,[14] coupled with conductive polymers, liquid metals, or conductive nanowire materials, which can follow the deformation without cracking. Another approach is to take advantage of established nonelastic substrate materials such as polyimides and parylene-C but patterned in structures that induce stretchability without introducing cracks in the conductive layer.[15,16] This approach exploits well-established 2D fabrication techniques and conductive materials such as metals.[5,17,18] Kirigami-inspired designs, for example, create mesh-like structures out of strategically placed cuts that leverage the bending of the material around each slit. This approach usually requires serpentine-like feedlines around the cuts to prevent high stress in the metal. Thus, it is best suited for approaches in which narrow feedlines can be fabricated or large patterning areas are available.[15,16] Another method for making a thin film stretchable is to deposit it onto an elastic prestretched substrate, thereby creating wrinkles and preventing stress from cracking the metal layer upon stretching. However, the resulting film might suffer from high internal stress in the relaxed state.[19–21] Building on the concept of wrinkles, where the film is made nonplanar to accommodate excess material, origami-inspired designs can enable the stretchability of flexible thin films by introducing folds. Typically, these folds are added postfabrication, resulting in only moderate fold density and consequently low stretchability, as well as high mechanical stress in the materials.[22–24]

To overcome the limitations above, folds can be introduced prefabrication by featuring them as the base substrate on top of which the layer-by-layer fabrication takes place. Hartmann et al. proposed the realization of prefolded conductors by using V-shaped etched silicon molds as substrates and exploiting the 3D conformal coating of parylene-C enabled by chemical vapor deposition (CVD).[25] Parylene-C is a polymer that has been shown to coat conformally and uniformly a large variety of shapes, even undercuts narrower than 200 nm.[26] This ap-

Figure 1. Fabrication steps. a) Schematic of the steps shown in cross-section. 1) 3D printing of the sinusoidal mold; 2) gelatin sacrificial layer via dip coating; 3) parylene-C coating via chemical vapor deposition (CVD); 4) gold sputtering; 5) laser patterning of feedlines; 6) coating of the second parylene-C layer with adhesion promoter; 7) laser cutting of the outline; 8) release of the electrodes in water. b) Photos of three exemplary stages of the process (scalebars 5 mm). I) The mold is printed; II) the gold feedlines are patterned; III) the electrode is ready and released from the mold.
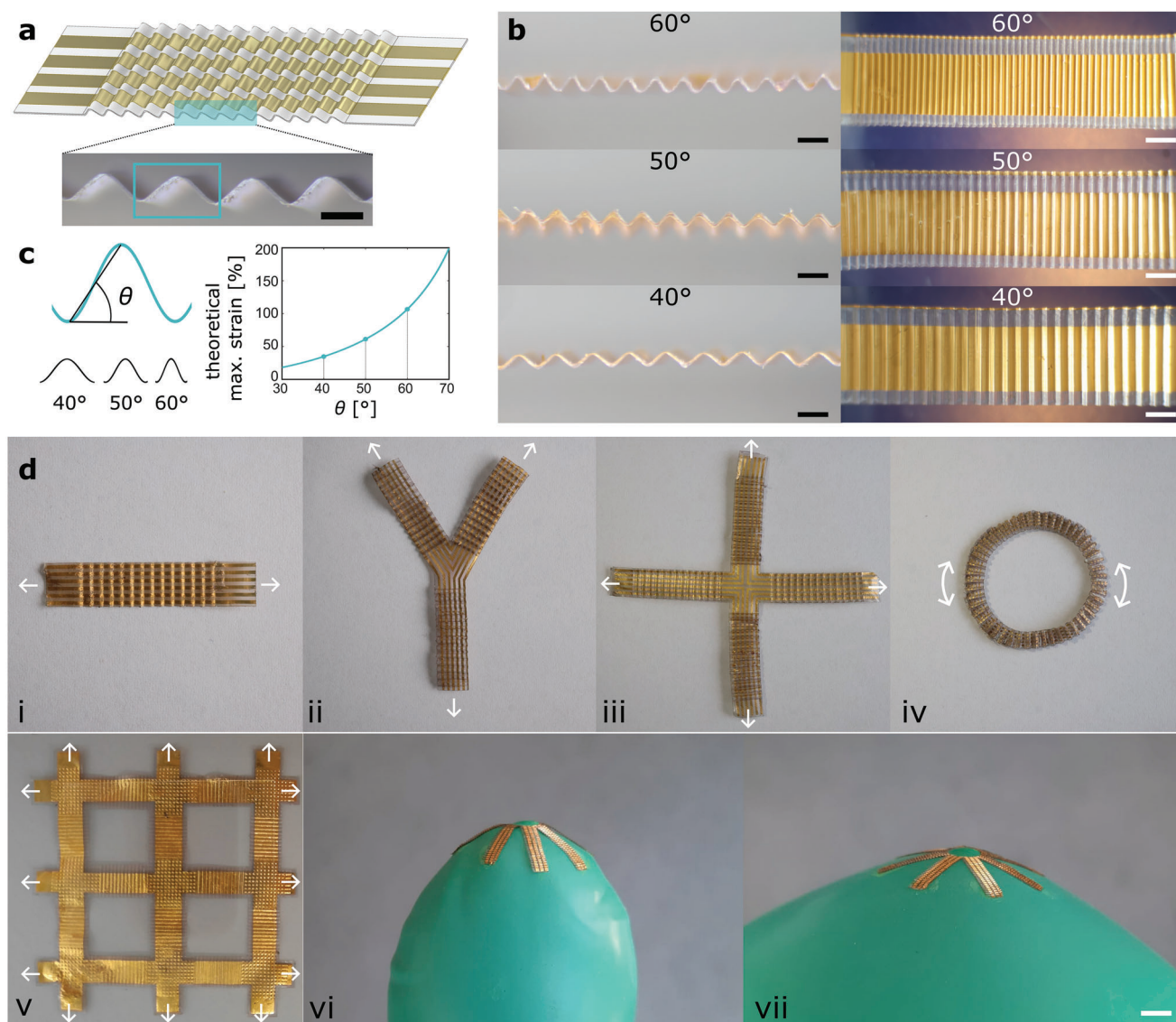
proach allowed for very high fold density and resolution, with stretchability being controlled by the design of the etched silicon mold, albeit following a geometry dictated by the crystal structure of silicon. Similarly, Kim et al. fabricated a stretchable dielectric film by thermally growing SiO_2 on a silicon mold etched into a wavy surface.[27] An alternative fabrication method to silicon processing is 3D printing—or additive manufacturing—which allows the rapid, easy, and cost-effective fabrication of 3D structures designed via computer-aided design (CAD) softwares, only at the price of lower achievable resolution.[28] Fabricating molds through 3D printing would thus broaden the range of designs in which prefolded electronics can be realized.

When patterning prefolded origami surfaces, there are a number of challenges to consider beyond just mold fabrication. In microelectromechanical systems (MEMS) fabrication, the standard technique for patterning is photolithography, which can achieve resolutions below 100 nm, depending on the setup.[29] However, photolithography has critical limitations for nonplanar substrates, one of which is the need for a uniform thickness of the photoresist layer over the whole surface. Some strategies have been proposed to overcome these challenges, such as using additional adhesion layers for dip coating or custom-made nebulizers for spray coating.[30,31] A major limitation of photolithography is the need for a precise focus of the UV light on the photoresist, which can be particularly challenging for nonplanar surfaces. While workarounds have been proposed for simple geometries such as cubic or curved substrates, these methods have required custom-made variations such as added rotors to expose all photoresist surfaces evenly.[31,32] They would become increasingly problematic given the depth and density of the envisaged 3D features involved for such molds. Laser ablation has been proposed as a fast and dry alternative to photolithography,[7,33,34] and laser markers often provide a 3D mapping feature to adjust the focus over known 3D designs.

In this work, we combine the prefolded fabrication strategy through CVD of parylene-C with the advantages of 3D printing for mold fabrication. A 3D printed mold allows direct control and design flexibility of the fold parameters, such as height, frequency, and steepness. Additionally, the direction of the folds can be chosen independently of the silicon crystal orientation. Stereolithography (SLA) is suitable as the 3D printing method due to its adequate compromise between resolution and printing time.[35] This approach offers an easy, fast fabrication process that does not require any wet etching step. Furthermore, we pattern the feedlines using laser ablation following the 3D substrate. We also explore the resolution limits of this patterning technique depending on the geometrical parameters of the prefolded substrates.

2. Results and Discussion

Folded electronics offer high compliance in dynamic environments, but devices are typically folded postfabrication, leading to high stress in the materials. Here, we present a technique to fabricate thin-film electrodes with custom-shaped prefolded origami architecture based on 3D printing and laser pattering. Introducing the folds in the film prefabrication is realized by using a mold with a series of grooves and ridges on top of which all fabrication steps take place. This approach is enabled by the use of vapor-deposited parylene-C as insulating polymer, which covers 3D surfaces conformally and homogeneously. Here, the molds are 3D printed, offering several advantages such as tunable fold height and steepness, and control over the directionality of the grooves. **Figure 1** shows the fabrication approach. Molds with a sinusoidal surface are 3D printed, surface-treated with O_2 plasma, and dip-coated in a water-soluble sacrificial layer. We chose gelatin because it is cost-effective, easily deposited, and fast soluble in water. The gelatin layer after drying has a measured thickness between 0.8 and 2 µm, therefore all present features in the range

Figure 2. Stretchable origami electrode. a) Illustration of the main electrode design and optical microscopy image of the folded structure that generates stretchability (scalebar = 0.5 mm). b) Optical microscopy images of the resulting electrodes with the three different angles: left, cross-sectional view, scalebar = 0.5 mm; right: top view, scalebar = 2 mm. c) Schematic of design parameters (left), theoretical maximum strain and its dependence on the angle steepness of the grooves (right). d) Images of various electrode designs and the corresponding enabled stretching direction: (in order) linear, three-way junction, four-way junction, ring, mesh, star (scalebar = 5 mm).
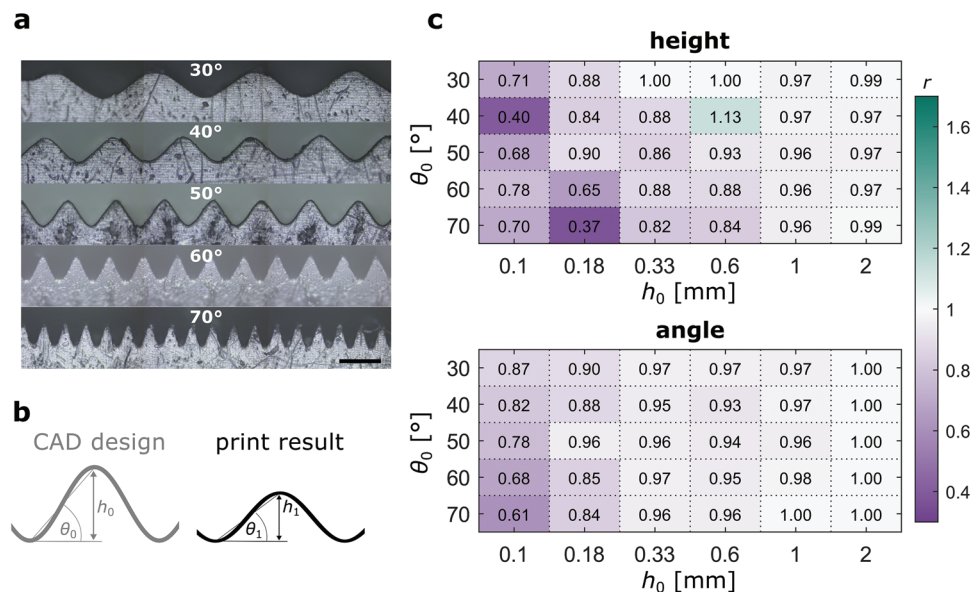
of 100 µm or larger are preserved. Plasma surface modification is necessary to increase the wettability of the mold and to ensure homogeneous gelatin coverage. After vacuum-drying the molds, parylene-C and gold are deposited. We used laser ablation with a 3D focus mapping feature to pattern the gold feedlines, then deposited the second layer of parylene-C and used the laser again to cut the electrode outline. We lastly released the samples from the molds by dissolving the sacrificial layer in 50 °C water. The free-standing devices exhibit the folds in a relaxed state, and can respond to applied forces by unfolding accordingly without stretching the thin film itself.

Figure 2 illustrates the design concept and resulting devices fabricated over a sinusoidally patterned mold, resulting in a cross-section, as seen in Figure 2a. In designing the molds, we aimed to maximize the stretchability of the resulting electrodes without compromising their manufacturability. Therefore, the design parameters chosen are the angle θ and the fold height h (Figure 2c) because they control the origami architecture's deformability and directly impact the fabrication results of 3D printing and laser patterning. In parametrizing the fabrication quality, we expected the prints' accuracy and the laser patterning's precision to decrease for steeper and deeper folds (i.e., for higher θ or h, respectively). Consequently, we express the fabrication results using these two geometrical parameters (see Section 2.1).

We can model the theoretical maximum strain of each design based on h and θ, where θ determines the number of folds

Figure 3. Accuracy analysis of 3D printed sinusoidal molds. a) Side-view microscopy images for molds of $h = 330\,\mu m$ (scalebar 500 µm). b) Schematic of the parameters taken for the calculation of the accuracy index. c) Accuracy index for both the height and the angle parameter.

per unit length (Figure 2c). In this model, the maximum achievable strain that generates no significant stretch in the material is considered to be reached when the sample is fully unfolded. This assumption is possible because of the nature of parylene-C, which is flexible as a thin film but not inherently stretchable due to its relatively low elastic strain limit (1.5%−2.8%).[36,37] The maximum length of the unfolded electrode per period is taken as the arc length of the sine wave in one period. The modeled strain is thus calculated as the percentage ratio between maximum deformation (electrode in the fully unfolded state) and original length (electrode in the relaxed folded state), as follows:

$$strain_\% \, (\theta, h) = \frac{L_{unfolded} - L_{relaxed}}{L_{relaxed}} \cdot 100$$

$$= \frac{\int_0^\lambda \sqrt{1 + \left(\pi \cdot \tan\theta \cdot \cos\left(\frac{\pi \cdot \tan\theta}{h} \cdot x \right) \right)^2} \, dx - \lambda}{\lambda} \cdot 100 \quad (1)$$
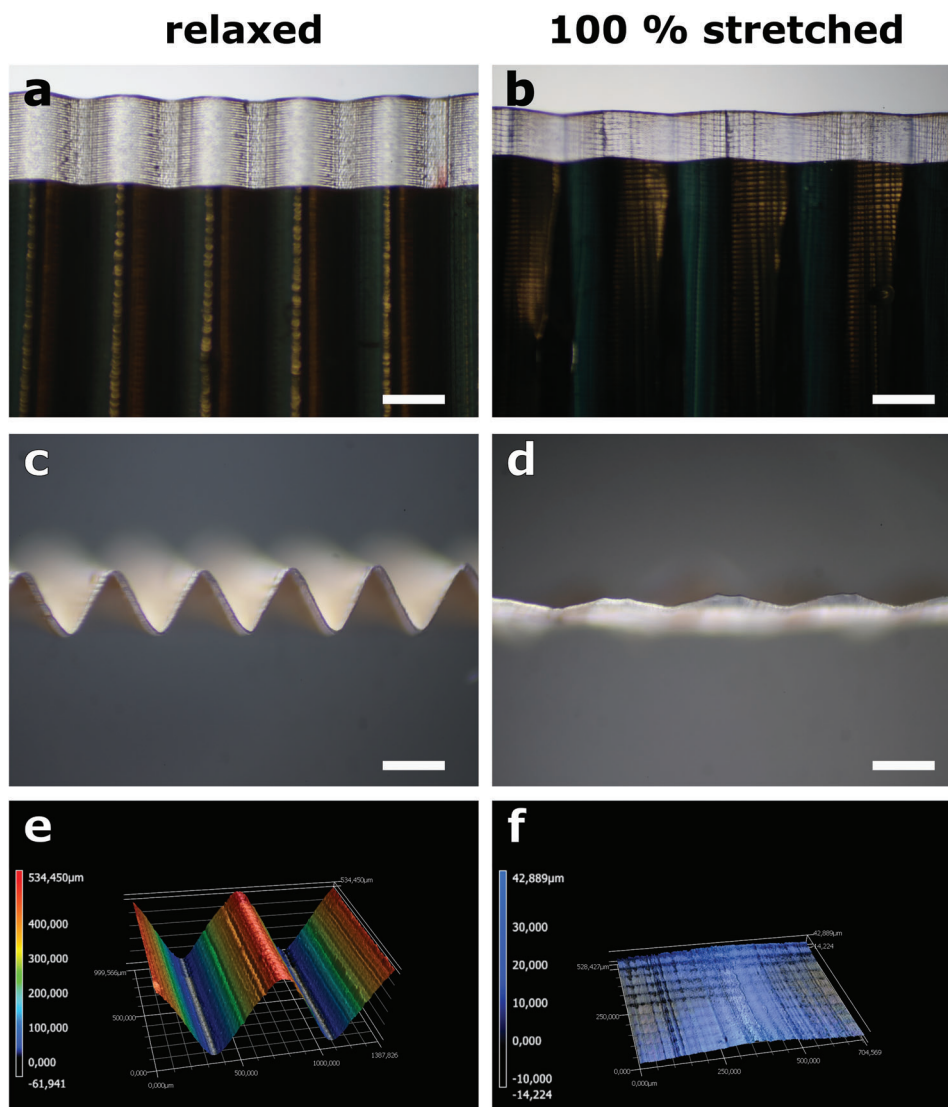
with $\lambda = \frac{2h}{\tan\theta}$ \quad (2)

where λ is the wavelength of the sine wave and depends directly on h and θ. Theoretically, the steeper the folds, the larger the strain up to which the device will remain functional. By adjusting the design parameters for folds as steep as 70°, we can achieve a theoretical maximum strain of up to ≈200%. In practice, there is an upper boundary to the steepness dictated by the resolution limits of SLA printing (see Section 2.1) and the laser patterning (see Section 2.3). Figure 2b shows electrodes fabricated with three different designs at 40°, 50°, and 60°. The steepness (or density) of the folds can be distinguished between the three electrodes in the relaxed state, from their cross-sectional and top view, respectively. The advantage of 3D printing for mold fabrication is demonstrated in Figure 2d. Starting from the linear design with

a constant direction of propagation, we can obtain bifurcations, intersections, and circular patterns by combinations of the same basic design. The custom direction of wave propagation provides complete control of the preferred directions of stretchability of the folded electrodes.

2.1. 3D Printing Accuracy

The quality of the molds is crucial for the successful fabrication of folded electrodes. The molds are 3D printed using SLA, which limits the smallest achievable features to an optical resolution of around 30 µm in the xy plane.[38] To identify the designs that would yield the highest printing accuracy, we fabricated molds at six different heights and five different angles, as presented in **Figure 3**. Figure 3a shows assembled microscopy images of the cross-section of molds with different angles θ for $h = 330\,\mu m$. The prints were fabricated with the sinusoidal cross-section placed on the xy plane to minimize the step-like artifact in the surface from layering. To quantitatively assess the resulting accuracy of the prints, the molds were imaged side view with a laser scanning microscope, and an accuracy index a was defined for each parameter x (angle, height) as shown in Figure 3b: $a_x = \frac{x_1}{x_0}$, where 0 and 1 indicate the nominal (CAD design) and measured (print) values of the two parameters, respectively.

With the definition above, $a_x = 1$ represents perfect accuracy. As shown in Figure 3c, the print accuracy results indicate that prints below 180 µm height often present significant deviations from the nominal values for both height and angle. These results indicate a lower limit of height features for designs with dense and slanted structures. Prints with angles steeper than 60° also resulted in lower accuracy since the resolution needed for the smallest features gets close to the limits of our SLA printer. On the other hand, prints with angles lower than 40° were considered inefficient in terms of resulting stretchability from the model. As

2300308 (4 of 9)

**ADVANCED
SCIENCE NEWS**

www.advancedsciencenews.com

**ADVANCED
ELECTRONIC
MATERIALS**

www.advelectronicmat.de

relaxed **100 % stretched**

Figure 4. Images of released electrodes. a,b) Optical images of a 60° sample electrode from the top, for both relaxed and stretched at 100% conditions (scalebars = 500 μm). c,d) Respective side views of the electrode (scalebars = 500 μm). e,f) 3D images obtained by laser scanning confocal microscopy.
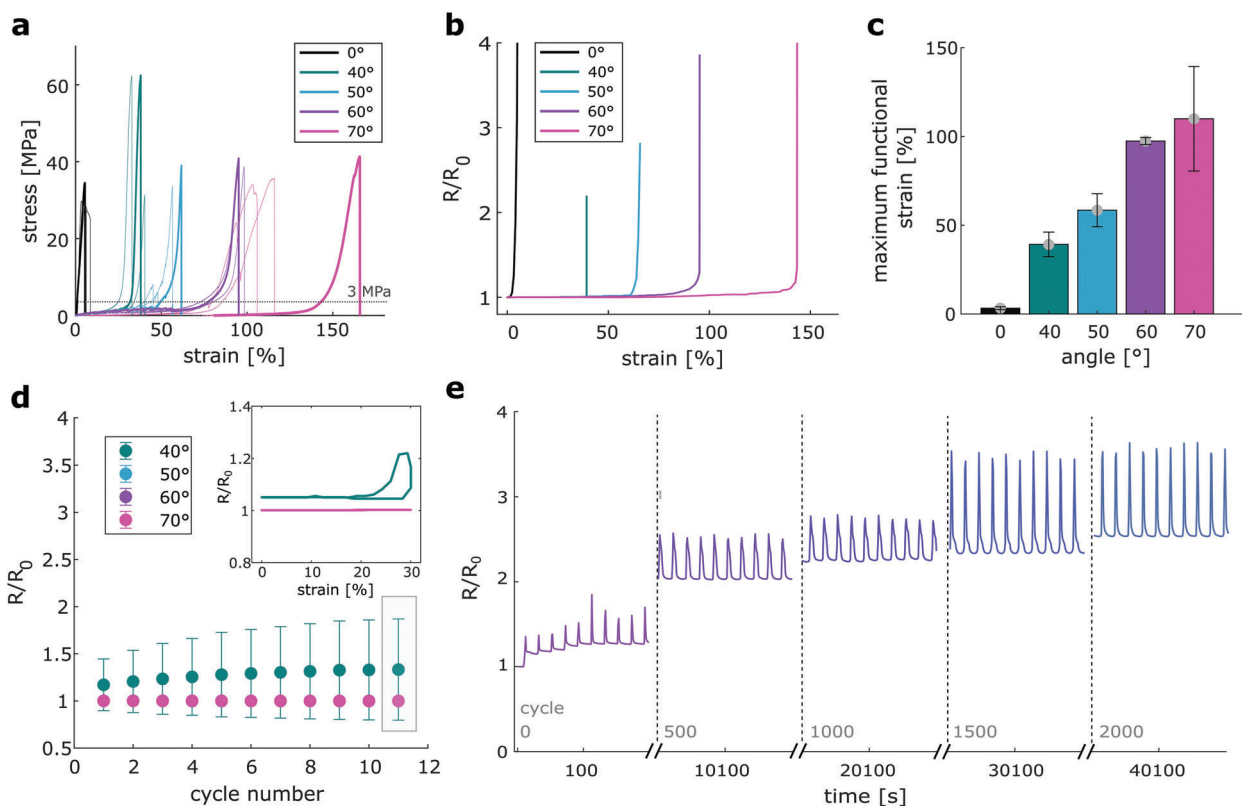
a result, we fabricated the electrodes for the electromechanical tests with angles of 40°, 50°, 60°, and 70°.

2.2. Stretchability

The structural stretchability mechanism of the released electrodes was initially verified using optical microscopy. **Figure 4** shows a sample electrode ($\theta = 40°$, $h = 600$ μm) in the relaxed state and at 20% strain, as seen in a top view (top), cross-sectional view (middle), and angled view taken via laser profilometry (bottom). The top view of the sample electrode (a, b) reveals the roughness of the resulting film. We examined the surface of an electrode fabricated over a flat mold printed analogously and compared it to a control electrode fabricated over a glass substrate. The average surface roughness (rms) of the sample from

the printed mold was found to be 1.7 ± 1.3 μm, compared to 0.26 ± 0.02 μm of the sample from the glass. This roughness is mainly due to the layer-by-layer printing, producing a step-like artifact in the result mainly along the printer's z-axis (the width of the mold), with each layer corresponding to 10 μm of mold width, observable in Figure 4a,b.

To verify the functionality of the devices during stretching, tensile measurements were made while simultaneously recording the electrical resistance between the two ends of the electrodes. **Figure 5** shows the results of the measurements conducted with the four designs of increasing steepness (40°, 50°, 60°, 70°) and $h = 600$ μm, compared to a control design of 0°. The folded architecture allows the electrodes to sustain strain with minimal applied stress and electrical resistance nearly unchanged until the fully unfolded state is reached. As can be seen in Figure 5a, the stress–strain curves show that electrodes with steeper folds

Figure 5. Electromechanical characterization results for electrodes of 600 μm height. a) Results of stress–strain measurements, showing all three samples per design, with one example trial per design highlighted. b) Example results of resistance–strain measurements, showing the corresponding example trial for each design. The resistance values are normalized over the initial resistance R_0 of each sample (average of first 10 s of recording). c) Maximum functional strain (strain values at which $R > 2R_0$) for each design, averaged over three samples (error bars show standard deviation). d) Resistance change for 10 cycles up to 30% strain, measured at the start of each cycle ($n = 3$ samples). The inset shows a resistance versus strain hysteresis curve of the last stretching cycle for each design. e) Long-term resistance behavior of a sample electrode with 60° angle, stretched up to 80% for more than 2000 cycles.
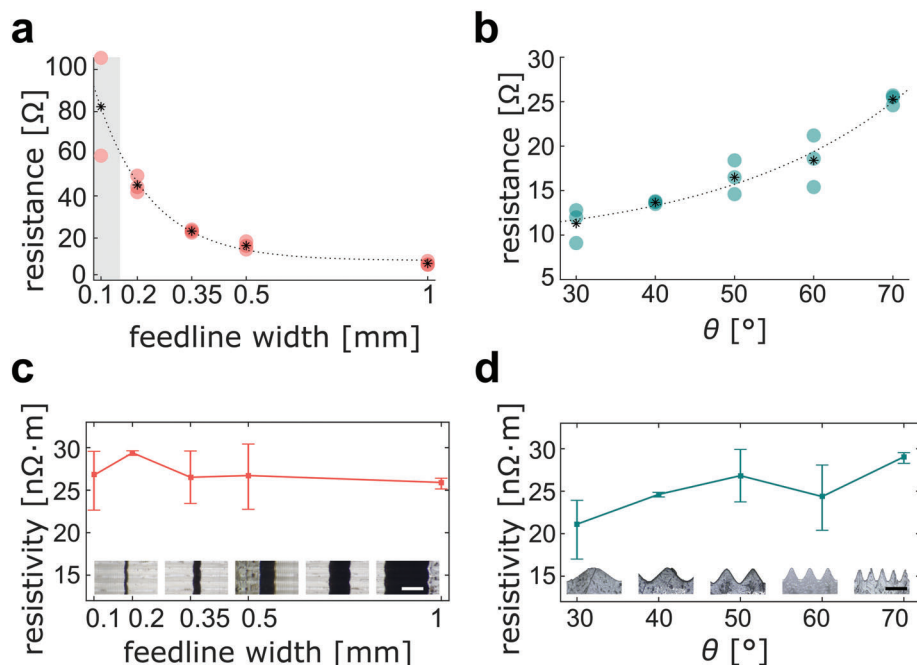
can withstand much higher strains while still experiencing minimal stress, e.g., lower than 3 MPa (or 0.18 N). Figure 5b shows the concurrent resistance measurement with respect to the applied strain. The resistance data was normalized to the initial resistance of each sample (ranging from 1.17 to 3.76 Ω), averaged from the first 10 s of recording at no applied strain. The electrical characterization reflects the results from the mechanical measurement of Figure 5a, in that the electrodes with steeper angles (and higher fold frequency) can withstand larger elongations before failure, i.e., being measured as an open circuit. Failure of the electrode when reaching the maximum theoretical strain occurs rapidly as parylene itself is not an inherently elastic material. Figure 5c shows the maximum functional strain, which we defined as the maximum strain at which the resistance $R < 2R_0$, for each design. We see that the maximum functional strain increases as expected with higher fold frequency. Changing the design from 40° to 50° angle expands the maximum functional strain from 40.6% to 59.9%. The measured strain limits are roughly in accordance with the respective theoretical maximum strains of 34.8% and 61.2%, predicted by the geometric model. For the 60° design, the measured strain goes up to 100.4%, compared to a predicted theoretical limit of 106.7%. For the 70° design, the maximum functional strain was measured

to be 109.9 ± 29.5%, thus much lower than the modeled maximum strain of 199.3%. The lower mean strain and large standard deviation of the measurement are due to the steepness of the features for the 70° samples. At higher angles, the fabrication of the electrodes becomes less reproducible, because the uniformity of the sacrificial layer and the precision of the laser cutting decrease.

We next investigated the electromechanical behavior of the electrodes undergoing repeated strain cycles. Figure 5d shows the change in resistance when the electrodes are stretched at 30% for 10 cycles, measured at the beginning of each cycle. We can see that the resistance increases by less than a factor of 2 for the 40° electrodes and stays unchanged for all the other designs. Figure 5e shows the long-term cyclic behavior of a 60° electrode repeatedly stretched at 80% strain (corresponding to ≈80% of the theoretical maximum limit). After 2000 cycles, the resistance has increased by a factor of 2.5.

2.3. Feedline Patterning Limits

We investigated the role of mold geometry over the feedline patterning via laser ablation. This method involves using a nanosec-

2300308 (6 of 9)

Figure 6. Limits of laser patterning for 3D electrode fabrication: a) Resistance changes over feedlines width laser patterned, for a geometry of 330 μm height and 50° angle. For 100 μm width and lower, most feedlines resulted not functioning (open circuit). The dashed line represents exponential fitting. b) Resistance changes over mold steepness, for feedlines of width 500 μm. c) Resistivity over feedline width: minimal influence of sinusoidal surface (scalebar = 0.5 mm). All data points show mean and std from $n = 3$ samples. d) Resistivity over feedline length: observable influence of wall steepness (scalebar = 0.5 mm).

ond pulsed UV laser (wavelength 355 nm, maximum output power 10 kW) to selectively remove the Au without damaging the parylene-C film, which still slightly absorbs UV radiation.[39] The power, scanning speed, repetitions, and shutter frequency of the laser have been optimized for the chosen materials. The laser scanner used provides a 3D mapping option so that the laser focus during scanning is matched with the 3D shape of the mold. The resolution for laser ablation is limited by the size of the laser spot. When patterning flat substrates, laser ablation has been shown to generate feedlines as small as 30 μm width for our laser system.[33] In the case of substrates with slanted features, such as sinusoidal grooves, we verified the patterning limits of the laser for feedlines running perpendicular to the grooves, both with respect to the smallest achievable width and the steepest patternable angle. **Figure 6**a shows the achievable feedline width for a sinusoidal mold of 300 μm height and 50° angle. For large widths (0.5–1 mm), the feedlines present low resistances between 10 and 20 Ω. The resistance increases as expected for smaller feedlines until starting to show a significant variance for widths ≤ 100 μm. As a result, our limit of feedline width patternable by laser ablation on sinusoidal molds was considered to be 200 μm. To verify that the change in resistance over feedline width was mainly due to the change in gold surface area, the resistivity was calculated (see Figure 6c). We can see that the resistivity varies only slightly for different widths, indicating that the laser patterning does not affect the resistance due to, e.g., edge artifacts. Figure 6b shows the resistance of 500 μm wide feedlines patterned over molds of different angles. As expected, the resistance increases for steeper angles, as the overall feedline length increases, i.e., the length in the unfolded state is higher. Here, we can notice that steeper

mold angles lead to higher calculated resistivity. This result can be attributed to the sputtering process, where the same amount of metal distributed over a larger surface area (depending on the frequency of the folds) yields a thinner deposited metal layer.

3. Conclusion and Outlook

We presented a new fabrication method for prefolded origami stretchable electrodes, utilizing 3D printed molds, conformal polymer coating, and laser patterning. This approach is fast and versatile, requiring no harsh chemical steps. By utilizing 3D printing technology, we were able to customize the geometries of the final electrodes with complete control over the designed stretching direction. Our approach also offers freedom on the parameters of the resulting folds, with limits only given by the printing layers and resolution. We demonstrated the fabrication of metal tracks over the 3D molds enabled by laser ablation, offering a simple, fast, and dry approach to the patterning of nonplanar structures. By adjusting geometrical parameters such as fold steepness, we were able to tune the structural stretchability of the resulting electrodes, achieving up to 100% strain with minimal resistance increase.

4. Experimental Section

Materials: Medicalprint mold clear 3D printing resin was obtained from Detax (Germany). Gelatin from bovine skin was purchased from Sigma–Aldrich (USA). 2-Propanol (≥99.5%) and ethanol (≥99.5%) were obtained from Carl Roth (Germany). Deionized water was generated

by a water purification system (Berry Tech, Germany). Parylene dimer (dichlorodi-p-xylylene) was obtained by Daisan Kasei Co., Ltd (Japan).

Molds 3D Printing: All molds were printed with MiiCraft 50 × 3D printer (MiiCraft, Taiwan) from CAD files designed in Inventor (2022, Autodesk, USA). The samples were printed in Medicalprint mold (brilliant-clear 2.0, Detax) with a layer height of 50 µm, an exposure time of 1.5 s per layer and 125% power. After printing, the molds were cleaned in 2-propanol in an ultrasonic bath for 5 min and blow dried. Finally, the molds were postcured in an Otoflash G171 UV-curing chamber (NK-Optic, Germany) with 2000 flashes under nitrogen flux.

Sacrificial Layer Coating: The sacrificial layer was prepared by diluting gelatin (2.5 g, Sigma–Aldrich) in deionized water (47.6 mL) in a glass bottle and left to dissolve on a hotplate at 50 °C for 4 h while magnetically stirring. The preparation was transferred in 2 mL Eppendorf tubes, spun for 90 s at 1200 rpm (miniSpin plus, Eppendorf, Germany), filtered with a 0.2 µm syringe filter (Whatman GD/X 13, Sigma–Aldrich) and transferred in a large petri dish. The surface of the molds was activated in oxygen plasma (Diener electronics GmbH, Germany) at 0.6 mbar and 80% power for 10 min. Each mold was fully immersed in the solution for 1 min at 50 °C, then was airdried at ambient conditions overnight.

Electrode Fabrication: A 5-µm-thick parylene-C layer was deposited via CVD (Plasma Parylene Systems, Germany) from the dimer precursor dichloro-di-p-xylylene (16.7 g, Daisan Kasei Co.). Then, a 160-nm-thick layer of Au was sputtered (35 mA, 3×10^{-2} mbar, Bal-tec MED 020, Germany) and patterned by a nanosecond pulsed laser scanner (MD-U1000, Keyence, Japan, 1000 mm s^{-1} scan speed, 7% power, 60 kHz repetition rate, 1 repetitions). The contact pads were masked by polyimide tape, then placed in the deposition chamber together with the adhesion promoter Silane A-174 (200 µL) for the top 5-µm-thick layer of parylene-C. The polyimide tape was removed, and the outline of the electrodes was laser-cut (MD-U1000, Keyence, 500 mm s^{-1} scan speed, 15% power, 40 kHz repetition rate, 50 repetitions). The electrodes were released by dissolving the gelatin layer in deionized water at 50 °C overnight.

Laser Microscopy: The molds were imaged with a 3D laser scanning microscope (20X, VK-X250, Keyence) and the results analyzed in Fiji (ImageJ 1.53t, USA).[40]

Optical Microscopy: Freestanding electrodes were placed in a linear module (Drylin, Igus GmbH, Germany) with 3D printed holders and stretched at different ratios. Images were taken with a bright-field microscope (Axioskop 2, Zeiss, Germany) and a camera (Canon EOS R5, Japan) both in a cross-sectional and a top view.

Electromechanical Testing: Tensile tests were conducted with a universal testing machine (TesT, Germany) with a 50 N load cell. The contact pads were covered with conductive copper tape to facilitate clamping, and the electrical resistance was measured with a digital multimeter (Fluke Corporation, USA). The strain limit was tested by stretching at a constant speed of 10 mm min^{-1} until rupture, after five consecutive conditioning cycles until 20% strain at a speed of 10 mm min^{-1}. The data was processed in MATLAB (MATLAB 2019b, MathWorks, USA).

Conflict of Interest

The authors declare no conflict of interest.

Author Contributions

F.D.D. conceived the research project, and B.W and L.H. provided input. F.D.D and B.W. designed the study. F.D.D. and R.F. fabricated and tested the devices, and L.H., G.B., and I.K. supported the fabrication. F.D.D prepared all figures. L.H, G.B., I.K., H.P., B.D.C, M.N., F.Z., and T.T. helped establish the fabrication techniques. F.D.D. wrote the main manuscript text, with support from B.W. and L.H. All authors reviewed the manuscript and provided critical feedback.

[1] Y. Hattori, L. Falgout, W. Lee, S. Y. Jung, E. Poon, J. W. Lee, I. Na, A. Geisler, D. Sadhwani, Y. Zhang, Y. Su, X. Wang, Z. Liu, J. Xia, H. Cheng, R. C. Webb, A. P. Bonifas, P. Won, J. W. Jeong, K. I. Jang, Y. M. Song, B. Nardone, M. Nodzenski, J. A. Fan, Y. Huang, D. P. West, A. S. Paller, M. Alam, W. H. Yeo, J. A. Rogers, *Adv. Healthcare Mater.* **2014**, *3*, 1597.

[2] Y. R. Jeong, G. Lee, H. Park, J. S. Ha, *Acc. Chem. Res.* **2019**, *52*, 91.

[3] T. R. Ray, J. Choi, A. J. Bandodkar, S. Krishnan, P. Gutruf, L. Tian, R. Ghaffari, J. A. Rogers, *Chem. Rev.* **2019**, *119*, 5461.

[4] G. Schwartz, B. C. K. Tee, J. Mei, A. L. Appleton, D. H. Kim, H. Wang, Z. Bao, *Nat. Commun.* **2013**, *4*, 1859.

[5] Y. Morikawa, S. Yamagiwa, H. Sawahata, R. Numano, K. Koida, M. Ishida, T. Kawano, *Adv. Healthcare Mater.* **2018**, *7*, 1701100.

[6] D. Qi, Z. Liu, M. Yu, Y. Liu, Y. Tang, J. Lv, J. Li, J. Wei, B. Liedberg, Z. Yu, X. Chen, *Adv. Mater.* **2015**, *27*, 3145.

[7] L. Hiendlmeier, F. Zurita, J. Vogel, F. D. Duca, G. A. Boustani, H. Peng, I. Kopic, M. Nikić, T. Teshima, B. Wolfrum, *Adv. Mater.* **2023**, *35*, 2210206.

[8] S. Lienemann, M. J. Donahue, J. Zötterman, S. Farnebo, K. Tybrandt, *Adv. Mater. Technol.* **2023**, *8*, 2201322.

[9] B. C. K. Tee, C. Wang, R. Allen, Z. Bao, *Nat. Nanotechnol.* **2012**, *7*, 825.

[10] A. Maziz, A. Concas, A. Khaldi, J. Stålhand, N.-K. Persson, E. W. H. Jager, *Sci. Adv.* **2017**, *3*, e1600327.

[11] K. Tybrandt, D. Khodagholy, B. Dielacher, F. Stauffer, A. F. Renz, G. Buzsáki, J. K. Vörös Tybrandt, B. Dielacher, F. Stauffer, A. F. Renz, J. Vörös, K. Tybrandt, D. Khodagholy, G. Buzsáki, *Adv. Mater.* **2018**, *30*, 1706520.

[12] D. Qi, K. Zhang, G. Tian, B. Jiang, Y. Huang, *Adv. Mater.* **2021**, *33*, 2003155.

[13] K. Terkan, F. Zurita, T. Jamal Khalaf, P. Rinklin, T. Teshima, B. Kohl, B. Wolfrum, *APL Mater.* **2020**, *8*, 101111.

[14] C. Larson, B. Peele, S. Li, S. Robinson, M. Totaro, L. Beccai, B. Mazzolai, R. Shepherd, *Science* **2016**, *351*, 1071.

[15] N. Matsuhisa, X. Chen, Z. Bao, T. Someya, *Chem. Soc. Rev.* **2019**, *48*, 2946.

[16] Y. Ma, X. Feng, J. A. Rogers, Y. Huang, Y. Zhang, *Lab Chip* **2017**, *17*, 1689.

[17] Z. Zhang, Y. Yu, Y. Tang, Y. shi Guan, Y. Hu, J. Yin, K. Willets, S. Ren, *Adv. Electron. Mater.* **2020**, *6*, 1900929.

[18] M. Isobe, K. Okumura, *Sci. Rep.* **2016**, *6*, 24758.

[19] Y. Zhu, F. Xu, X. Wang, Y. Zhu, *Adv. Funct. Mater.* **2012**, *22*, 1279.

ADVANCED
SCIENCE NEWS

www.advancedsciencenews.com

ADVANCED
ELECTRONIC
MATERIALS

www.advelectronicmat.de

[20] Y. Zhu, F. Xu, *Adv. Mater.* **2012**, *24*, 1073.

[21] A. Takei, S. Tsukamoto, Y. Komazaki, Y. Kusaka, K. Kuribara, M. Yoshida, *AIP Adv.* **2020**, *10*, 25205.

[22] Z. Qi, M. Zhou, Y. Li, Z. Xia, W. Huo, X. Huang, *Adv. Mater. Technol.* **2021**, *6*, 2001124.

[23] C. H. Lin, D. S. Tsai, T. C. Wei, D. H. Lien, J. J. Ke, C. H. Su, J. Y. Sun, Y. C. Liao, J. H. He, *ACS Nano* **2017**, *11*, 10230.

[24] Z. Song, T. Ma, R. Tang, Q. Cheng, X. Wang, D. Krishnaraju, R. Panat, C. K. Chan, H. Yu, H. Jiang, *Nat. Commun.* **2014**, *5*, 3140.

[25] F. Hartmann, M. Jakešová, G. Mao, M. Nikić, M. Kaltenbrunner, V. Đerek, E. D. Głowacki, *Adv. Electron. Mater.* **2021**, *7*, 2001236.

[26] Y. Li, Q. Xie, W. Wang, M. Zheng, H. Zhang, Y. Lei, H. A. Zhang, W. Wu, Z. Li, *J. Micromech. Microeng.* **2011**, *21*, 067001.

[27] H. Kim, G.-S. Hwang, S. Lee, J.-Y. Kim, *Adv. Electron. Mater.* **n.d.**, *n/a*, 2300078.

[28] S. Kumar, P. Bhushan, M. Pandey, S. Bhattacharya, *J. Micromanuf.* **2019**, *2*, 175.

[29] L. Zheng, U. Zywietz, T. Birr, M. Duderstadt, L. Overmeyer, B. Roth, C. Reinhardt, *Microsyst. Nanoeng.* **2021**, *7*, 64.

[30] J. Lim, A. R. Kim, S. Kim, S. Lee, D. Yoo, J. Park, J. Kim, *Adv. Mater. Interfaces* **2019**, *6*, 1901485.

[31] K. Yamazaki, H. Namatsu, *Jpn. J. Appl. Phys., Part 2* **2006**, *45*, L403.

[32] J. Park, H. Fujita, B. Kim, *Sens. Actuators, A* **2011**, *168*, 105.

[33] H. Peng, L. Grob, L. J. K. Weiß, L. Hiendlmeier, E. Music, I. Kopic, T. F. Teshima, P. Rinklin, B. Wolfrum, *Nanoscale* **2023**, *15*, 4006.

[34] N. Tandon, A. Marsano, R. Maidhof, K. Numata, C. Montouri-Sorrentino, C. Cannizzaro, J. Voldman, G. Vunjak-Novakovic, *Lab Chip* **2010**, *10*, 692.

[35] S. Choo, S. Jin, J. Jung, *Pharmaceutics* **2022**, *14*, 766.

[36] C.-L. Chen, E. Lopez, Y.-J. Jung, S. Müftü, S. Selvarasah, M. R. Dokmeci, *Appl. Phys. Lett.* **2008**, *93*, 093109.

[37] X. Chai, J. Liu, Q. He, G. Peng, C. Yang, *Appl. Surf. Sci.* **2011**, *257*, 10771.

[38] J. Z. Manapat, Q. Chen, P. Ye, R. C. Advincula, *Macromol. Mater. Eng.* **2017**, *302*, 1600553.

[39] M. Bera, A. Rivaton, C. Gandon, J. L. Gardette, *Eur. Polym. J.* **2000**, *36*, 1765.

[40] J. Schindelin, I. Arganda-Carreras, E. Frise, V. Kaynig, M. Longair, T. Pietzsch, S. Preibisch, C. Rueden, S. Saalfeld, B. Schmid, J.-Y. Tinevez, D. J. White, V. Hartenstein, K. Eliceiri, P. Tomancak, A. Cardona, *Nat. Methods* **2012**, *9*, 676.